Leucine zipper-based SAIM imaging identifies therapeutic agents to disrupt the cancer cell glycocalyx for enhanced immunotherapy

Sangwoo Park[1,2,7,8], Justin H. Paek[3,8], Marshall J. Colville[2], Ling-Ting Huang[2], Audrey P. Struzyk[3], Sydney J. Womack[6], Sriram Neelamegham[5], Heidi L. Reesink[6], Matthew J. Paszek[1,2,3,4#]

[1]Graduate Field of Biophysics, Cornell University, Ithaca, NY, USA

[2]Robert Frederick Smith School of Chemical and Biomolecular Engineering, Cornell University, Ithaca, NY, USA

[3]Nancy E. and Peter C. Meinig School of Biomedical Engineering, Cornell University, Ithaca, NY, USA

[4]Kavli Institute at Cornell for Nanoscale Science, Cornell University, Ithaca, NY, USA

[5]State University of New York, Buffalo, NY, USA

[6]Department of Clinical Sciences, College of Veterinary Medicine, Cornell University, Ithaca, NY, USA

[7]Current address: Cellular Immunotherapy Program, Cancer Center, Massachusetts General Hospital and Harvard Medical School, Boston, MA

[8]These authors contributed equally to this work

[#]To whom correspondence should be addressed: mjp31@cornell.edu

Abstract

The abnormally thick glycocalyx of cancer cells can provide a physical barrier to immune cell recognition and effective immunotherapy. Here, we demonstrate an optical method based on Scanning Angle Interference Microscopy (SAIM) for the screening of therapeutic agents that can disrupt the glycocalyx layer as a strategy to improve anti-cancer immune responses. We developed a new membrane labeling strategy utilizing leucine zipper pairs to fluorescently mark the glycocalyx layer boundary for precise and robust measurement of glycocalyx thickness with SAIM. Using this platform, we evaluated the effects of glycosylation inhibitors and targeted enzymatic degraders of the glycocalyx, with particular focus on strategies for cholangiocarcinoma (CCA), a highly lethal malignancy with limited therapeutic options. We found that CCA had the highest mean expression of the cancer-associated mucin, MUC1, across all cancers represented in the cancer cell line encyclopedia. Pharmacological inhibitors of mucin-type O-glycosylation and mucin-specific proteases, such as StcE, could dramatically reduce the glycocalyx layer in the YSCCC model of intrahepatic CCA. Motivated by these findings, we engineered Natural Killer (NK) cells tethered with StcE to enhance NK cell-mediated cytotoxicity against CCA. In a CCA xenograft model, these engineered NK cells demonstrated superior anti-tumor efficacy compared to wild-type NK cells, with no observable adverse effects. Our findings not only provide a reliable imaging-based screening platform for evaluating glycocalyx-targeting pharmacological interventions but also offer mechanistic insights into how CCA may avoid immune elimination through fortification of the glycocalyx layer with mucins. Additionally, this work presents a novel therapeutic strategy for mucin-overexpressing cancers, potentially improving immunotherapy efficacy across various cancer types.

Introduction

The cellular glycocalyx is a dense meshwork of glycosylated macromolecules that covers all eukaryotic cell surfaces. As the first point of contact between two interacting cells, the glycocalyx constitutes a vital component of cell-cell interfaces, including immune synapses formed between immune effector cells and target cancer cells. Oncogenesis is commonly accompanied by the dysregulated expression of various glycosyltransferases, resulting in a remodeling of the glycan landscape presented at the cell surface. Additionally, many tumors are associated with the overexpression of bulky, hydrating glycopolymers, such as cell-surface mucins and glycosaminoglycans (GAGs), which cause a swelling and thickening of the glycocalyx[1]. Cells that have undergone malignant transformation therefore exhibit marked changes in both the molecular composition and physical architecture of the glycocalyx, transforming it into a form of armor that can protect them against surveilling immune cells[2–6].

Thus far, development of immunotherapeutic strategies to overcome the cancer glycocalyx has largely been shaped by research efforts to identify tumor-specific glycan signatures that biochemically suppress cytolytic immune cell activity. Accordingly, most strategies to counter glycocalyx-mediated immune evasion focus on blocking the biochemical signaling pathways that are activated by carbohydrate-binding receptors. These strategies includes the pharmacological inhibition of the biosynthesis of glyco-immune checkpoint ligands[6–8], antibody-mediated blockade of the receptors for these ligands[9,10], and the targeted degradation of cancer-associated mucins or other glycoproteins that carry these ligands[11,12]. However, evaluating the efficacy of new glycocalyx-targeting therapeutics based on biochemical activation alone is not sufficient for predicting enhancement to immune cell-mediated killing. For example, our previous work has demonstrated that the dense polymer layer formed by overexpression of the cell-surface mucin, MUC1, acts as a physical barrier to immune cell attack, offering protection from immune cells even when they are equipped with chimeric antigen receptors (CARs) to enhance their biochemical activation[13]. Notably, nanometer-scale reductions in the glycocalyx thickness can severely compromise the ability of cancer cells to evade elimination by cytotoxic immune cells[13]. These findings suggest a potential new form of anticancer immunotherapy based on therapeutic strategies that disrupt the physical structure of the glycocalyx or its biosynthesis.

Some of the most lethal solid tumor cancers express high levels of cell surface mucins and respond poorly to current immunotherapies. As one important example, cholangiocarcinoma (CCA) is a heterogeneous group of aggressive malignancies arising from different locations within the biliary tree[14]. MUC1 expression in CCA is closely correlated with dedifferentiation, invasion, and poor patient survival[15]. The malignancy often presents challenges in early detection due to its asymptomatic nature in the initial stages, leading to a grim prognosis upon diagnosis. Advanced CCA typically carries a dismal prognosis, with surgical resection being the primary curative approach, albeit feasible only in a minority of cases due in part to the complexity of the bile duct system and often diffuse nature of tumors[16]. Response rates of CCA to current immunotherapies remain disappointingly low[17]. Only limited success has been achieved with checkpoint blockade, and CCA generally lacks suitable target antigens for CAR-based cellular immunotherapies. Whether disruption of the physical structure of the glycocalyx layer could improve immune responses in CCA remains untested.

One major roadblock to the development of glycocalyx-disrupting agents is a general lack of adequate tools that enable the precise characterization of how the individual molecular constituents of the cancer glycocalyx affects its nanoscale structure. To this end, Möckl et al. has coupled metabolic labeling of glycans with single molecule localization microscopy (SMLM) to show that the height of the glycocalyx increases in correspondence with key programs in malignancy, such as the epithelial-to-mesenchymal transition and oncogenic Ras activation[18]. However, the utility of SMLM for drug screening and development is limited by slow acquisition times on the order of 1-30 minutes per cell, reducing sample throughout and typically restricting imaging to fixed samples[19]. Chemical fixation in SMLM and other high resolution imaging techniques, such as electron microscopy, can introduce artifacts that may alter the native glycocalyx architecture, complicating the ability to detect nanometer-scale changes in glycocalyx structure. A robust technique that can be used to rapidly assess how the nanoscale structure of the glycocalyx in live cells responds to drug perturbations is necessary to accelerate the discovery of new therapeutic agents that target the glycocalyx.

As one potential solution, our group has advanced an optical technology termed Scanning Angle Interference Microscopy (SAIM) for high-speed and precise measurement of the glycocalyx thickness[13]. Based on the principles

83 of fluorescence interference contrast microscopy, SAIM can accurately measure the nanoscale space occupied by

84 the glycocalyx between the plasma membrane and a substrate. With its sub-second acquisition rate, SAIM has strong

85 potential for screening the effects of drug compounds on the glycocalyx structure. However, the robust application

86 of SAIM across a broad range of cancer cell types has been limited by challenges in achieving stable and specific

87 labeling of the plasma membrane, which is used to mark the boundary of the glycocalyx layer. For example,

88 fluorescent proteins expressed on the cell membrane via genetic approaches often show intracellular retention in

89 Golgi or endoplasmic reticulum (ER), disrupting the interference pattern of SAIM and compromising accuracy[20].

90 Additionally, lipophilic membrane dyes frequently fail to maintain surface localization and undergo rapid endocytic

91 internalization. Furthermore, heterogeneity in the lipid compositions of the membranes across cell lines and even

92 within the same model can affect the labeling efficiency of lipophilic dyes, requiring painstaking optimization of

93 labeling conditions for each cell line[21,22]. Therefore, a need remains for an alternative strategy that enables efficient,

94 long-lasting, and specific fluorescent labeling of the plasma membrane of any cell with minimal toxicity to cells

95 over the course of a SAIM imaging experiment.

96 In this study, we report the development of a novel method of fluorescently labeling the plasma membranes of live

97 cells by utilizing engineered coiled-coil dimerization pairs. By genetically engineering target cells to display a

98 leucine zipper and recombinantly producing the cognate leucine zipper fused to a fluorescent dye, we achieve highly

99 specific, robust labeling of the plasma membrane in a wide range of cancer cell lines. This approach demonstrated

100 superior membrane retention and labeling efficiency compared to conventional lipophilic dyes, enabling precise

101 quantification of glycocalyx thickness across diverse cancer cell types with SAIM. Using this platform, we

102 systematically evaluated glycocalyx responses to pharmacological and enzymatic perturbations in a CCA culture

103 model and identified agents that are highly effective at reducing glycocalyx thickness. From this initial screen, we

104 further evaluated the most promising candidates for their ability to enhance immune cell-mediated killing *in vitro*,

105 which informed the development of an anti-CCA cell-based immunotherapy that utilizes an enzymatic degrader.

106 Lastly, we established a CCA xenograft model to test our cell-based therapeutic, which demonstrated pronounced

107 efficacy *in vivo*.

Results

Development and validation of a leucine zipper-based membrane labelling strategy for stable SAIM imaging

Our previous work identified the importance of a single physical parameter of the cancer glycocalyx, its material thickness, as a strikingly strong predictor of tumor cells' ability to evade immune cell attack[13]. The strong dependence of cancer cell survival on glycocalyx thickness motivated us to search for compounds that can be used to "deflate" the cancer cell glycocalyx and accordingly, enhance immune cell killing (**Fig. 1a**). This required an approach to accurately measure glycocalyx thickness in live cells with nanoscale precision. To this end, we have developed Scanning Angle Interference Microscopy (SAIM), which enables nanoscale axial localization of fluorescent dyes[13,18,23–26] (**Fig. 1b**). However, SAIM-based measurement of the glycocalyx requires stable and specific labeling of the plasma membrane, which marks the boundary of the glycocalyx layer (**Fig. 1b**).

To improve the robustness of SAIM for drug screening applications, we developed a more optimal membrane-labeling strategy utilizing engineered leucine zipper dimerization motifs, previously validated for its high specificity and stability[27–29]. The leucine zipper pair, which we refer to as "Azip" and "Bzip", is comprised of several heptad repeats that favorably interact through a combination of electrostatic and hydrophobic interactions, resulting in binding with low nanomolar affinity (**Fig. 1c**). To specifically label the plasma membrane, we engineered target cells to display Bzip on the cell surface using the PDGFRβ transmembrane (TM) domain via lentiviral transduction, then recombinantly produced Azip fused to superfolder GFP (sfGFP) to be used as a membrane-labeling probe (**Fig. 2a,b**). To confirm successful lentiviral transduction and enable fluorescence-based sorting of target cells, Bzip constructs contained either an ALFA tag or mScarlet-i (**Fig. 2a**). This approach successfully enabled bright and specific membrane labeling with Azip-sfGFP across all tested cancer cell lines, including the pancreatic cancer cell line Capan-2 and the breast cancer cell lines KPL-1, T47D, SKBR3, and ZR-75-1 (**Fig. 2c,d**). Notably, expression of direct fusion of mScarlet to Bzip was not sufficient to achieve highly specific labeling of the cell surface, since mScarlet also fluoresced brightly in various intracellular organelles (**Fig. 2d**). We observed that the Azip-sfGFP probe was often excluded from the tight intercellular junctions within cancer cell colonies (**Fig. 2d**). We noted that this could limit the utility of the Azip probe for SAIM measurements, which requires a high density of fluorophores

133   to penetrate the glycocalyx in the small cleft between the plasma membrane and the imaging substrate. To optimize

134   the system further, we replaced the fluorescent protein markers on Azip with smaller and more efficient organic

135   dyes through sortase-mediated conjugation (**Fig. 2e**). By inserting a sortag sequence between Azip and sfGFP, we

136   enabled conjugation of small organic fluorophores (AF488 or AF647) to the purified Azip construct (**Fig. 2f**). This

137   refined strategy reduced the size of the Azip probe from ~35 kDa to ~7 kDa, and demonstrated strong and specific

138   binding to Bzip-expressing cancer cells with negligible background binding (**Fig. 2g,h**). We also observed that the

139   Azip dye conjugated with AF488 or AF647 penetrated intercellular junctions in cancer cells more effectively than

140   the sfGFP conjugate (**Fig. 2h**)

141   To optimize and validate the labeling efficacy of our membrane dye, we tested its performance under various

142   staining conditions optimized for SAIM imaging. We compared standard cold labeling (4°C, 1 hour) with rapid

143   warm labeling (37°C, 10 minutes), finding that the Azip dye demonstrated significantly improved membrane

144   retention without endocytosis even in warm labeling conditions (**Fig. 2h and Extended Data Fig. 1**). Long-term

145   stability was assessed over 48 hours and showed that Azip-based dyes exhibited significantly higher plasma

146   membrane retention and minimal intracellular uptake compared to popular lipophilic dyes, including DiO, CellBrite,

147   and MemGlow[30] (**Fig. 2i-k**). While Azip conjugated with AF647 showed minor endocytosis after 48 hours, Azip-

148   AF488 maintained remarkably stable plasma membrane localization throughout the extended imaging period,

149   establishing it as an optimal tool for dynamic SAIM imaging applications.

150   **Cholangiocarcinoma cell line YSCCC exhibits high MUC1 surface expression**

151   Having established a robust method for membrane labeling, we next sought to survey a broad range of cancer cell

152   lines that could serve as models for glycocalyx-mediated immune avoidance. Given that cell-surface MUC1

153   expression levels are strong determinants of the glycocalyx layer thickness[13], we sought to identify cancer cell types

154   and associated cell line models with high MUC1 overexpression. Analysis of publicly available datasets from the

155   DepMap project revealed that CCA exhibits the highest mean MUC1 RNA expression levels compared to other

156   tumor types (**Fig. 3a**). To investigate the correlation between MUC1 transcript levels and MUC1 protein density on

157   the cell surface, we conducted an analysis across various human cancer cell lines using a monoclonal anti-MUC1

158 antibody (clone HMPV) that specifically recognizes a core peptide in the VNTR region of MUC1 in a glycosylation-

159 independent manner. For standardization across experiments, we utilized the SKBR3 cell line as a reference control

160 in each experimental replicate and normalized the median fluorescence intensity (MFI) of test cell lines to that of

161 SKBR3. Linear regression analysis of normalized MFIs against MUC1 RNA transcript levels from the DepMap

162 project demonstrated a strong correlation (R^2 = 0.7768) (**Fig. 3b**). Notably, among the panel of cell lines tested,

163 YSCCC intrahepatic CCA cells exhibited the highest MUC1 surface expression, which strongly correlated with

164 their elevated MUC1 transcript levels.

165 Since there are relatively few reports on the YSCCC intrahepatic CCA model in the literature, we characterized the

166 adhesive and morphological phenotypes of the cell line. Interestingly, we observed that YSCCC cells in culture

167 exist as a mixed population of adherent and suspended cells, suggesting the presence of a substantially repulsive

168 glycocalyx that potentially impairs cell-substrate adhesion[31,32]. To test this hypothesis, we challenged YSCCC cells

169 to adhere to standard tissue culture plates overnight in either the presence or absence of a low dose (1 nM) of mucin-

170 digesting enzymes, StcE and SmE, which are known to broadly cleave mucin-domain glycoproteins from the cell

171 surface[33–35]. Following overnight treatment with the mucinases at 37°C, YSCCC cells showed significantly reduced

172 cell-surface MUC1 levels compared to untreated controls (**Fig. 3c**). Morphological analysis revealed that untreated

173 YSCCC cells exhibited partial adherence and spreading on culture plates, with a substantial proportion maintaining

174 a highly circular morphology and poor adhesion (**Fig. 3d-g**). In contrast, mucinase-treated cells demonstrated

175 increased spreading area and a significantly reduced proportion of circular cells (**Fig. 3e-g**). Notably, SmE treatment

176 showed relatively modest effects, consistent with only partial MUC1 cleavage under the lower concentration

177 protocol.

178 Aside from disrupting cell-substrate adhesion, we reasoned that a highly repulsive glycocalyx could also prevent

179 cell-cell adhesion, an essential step in immune cell-mediated elimination of cancer cells. To evaluate the impact of

180 the cellular glycocalyx on cell-cell adhesion, we assessed the capacity of YSCCC cells to form compact

181 multicellular clusters in ultra-low attachment wells. We hypothesized that cells with high repulsive forces would

182 resist forming close cell-cell contacts, resulting in increased intercellular spacing within aggregates as predicted

183   previously[31,36] (**Fig. 3h**). YSCCC cells cultured for 24 hours in ultra-low attachment wells demonstrated minimal

184   cell-cell association, forming diffuse aggregates at the well bottom. However, treatment with StcE mucinase

185   significantly reduced cell-cell repulsion, enabling intercellular adhesion and resulting in more compact aggregate

186   formation (**Fig. 3i,j**). These findings suggest that reduction in MUC1 levels through enzymatic treatment promotes

187   a more adherent and spread morphology in YSCCC cells.

188   **Screening glycocalyx-degrading agents using leucine zipper-based SAIM**

189   Pharmacological inhibitors have demonstrated promising outcomes in inhibiting O-glycan biosynthesis or

190   eliminating sialylation on cell membranes, which significantly influences cancer cell adhesion and invasion[37,38].

191   However, a systematic evaluation of pharmacological inhibitors and glycocalyx-degrading enzymes for their

192   specific ability to reduce glycocalyx thickness in cancer cells has not yet been performed. We investigated a

193   peracetylated N-thioglycolyl modified N-acetylgalactosamine (GalNAc) analog ($Ac_5GalNTGc$) that has been

194   shown to interfere with O-glycan extension through GalNAc-mediated core-1 synthesis inhibition[39–41]. We also

195   tested the pan-sialyltransferase inhibitor, $P-3F_{AX}$-Neu5Ac, which depletes α2,3-/α2,6-linked sialic acids without

196   affecting cell viability or proliferation[42,43] and reduces tumor growth *in vivo* [43]. Following the validation of our

197   membrane labeling strategy, we implemented the leucine zipper-based SAIM imaging approach to quantitatively

198   measure glycocalyx thickness across different cells lines, including YSCCC and the breast cancer cell lines, SKBR3

199   and KPL-1 as additional examples (**Extended Data Fig. 2a-c**). Cells engineered to express the Bzip construct were

200   cultured on fibronectin-coated silicon wafers and labeled with Azip-AF488 for 10 minutes at 37°C. As expected,

201   Azip-AF488 effectively penetrated the space between the cell membrane and imaging substrate in all cell types,

202   generating well-defined interference patterns that enabled precise mapping of the glycocalyx thickness with

203   nanometer resolution (**Fig. 4** and **Extended Data Fig. 2**).

204   We next investigated how the pharmacological inhibitors of glycosylation and an enzymatic degrader affect the

205   glycocalyx structure in YSCCC cancer cells (**Fig. 4a**). Using the leucine zipper-based strategy to mark the

206   membrane for SAIM, we measured changes in glycocalyx thickness in YSCCC cancer cells treated with

207    $Ac_5GalNTGc$, $P-3F_{AX}$-Neu5Ac, and StcE mucinase (**Fig. 4b**). Clear shifts in the pixel-wise SAIM interferograms

208   were observed following inhibition of glycosylation or enzyme-mediated degradation of mucins, indicating a

209   measurable change in glycocalyx thickness (**Fig. 4c**). In YSCCC cells, the average glycocalyx thickness decreased

210   from 96 ± 16 nm to 83 ± 16 nm after 48 hours of Ac$_5$GalNTGc treatment, an average reduction of 13 nm. Treatment

211   with 100 nM StcE mucinase resulted in a glycocalyx thickness of 77 ± 10 nm, corresponding to a reduction of 19

212   nm (**Fig. 4d**). Notably, YSCCC treatment with the sialylation inhibitor, P-3F$_{AX}$-Neu5Ac, did not significantly reduce

213   the glycocalyx thickness compared to untreated controls. These results demonstrate that leucine zipper-based

214   membrane labeling combined with SAIM imaging provides a reliable screening platform for assessing how

215   potential therapeutic agents alter the glycocalyx structure.

216   We considered the generality of our findings by testing the effects of inhibitors on an additional cell line, KPL-1.

217   While the average glycocalyx thickness in DMSO-treated control KPL-1 cells was 67 ± 7 nm, it decreased by an

218   average of 21 nm to 46 ± 9 nm after 48 hours of treatment with Ac$_5$GalNTGc (**Extended Data Fig. 2d,e**). Treatment

219   with P-3F$_{AX}$-Neu5Ac reduced glycocalyx thickness to 28 ± 7 nm, representing an even larger decrease of 40 nm.

220   This suggests that the glycocalyx structure of KPL-1 cells is markedly more sensitive to the sialylation inhibitor

221   compared to YSCCC (**Fig. 4d and Extended Data Fig. 2e**). To assess glycosylation capacity in KPL-1 and YSCCC,

222   transcriptomic data was used to reconstruct biosynthetic pathways in GlycoMaple, a glycosylation mapping tool

223   that has been reported to estimate glycan structures in cells based on gene expression (**Extended Data Fig. 3,4**)[44].

224   Although KPL-1 were predicted to have somewhat higher capacity for polysialic acid biosynthesis, sialylation

225   capacity was largely comparable between KPL-1 and YSCCC. Thus, the greater response of the KPL-1 glycocalyx

226   to sialylation inhibition would not have been predicted by gene expression alone. YSCCC were predicted to have a

227   higher capacity for biosynthesis of more extended and complex core-2 O-glycans, which may in part explain their

228   sensitivity to inhibition with Ac$_5$GalNTGc. Collectively, these results suggest that the response to interference

229   strategies may be cancer cell type specific and difficult to predict, emphasizing the need for the direct measurement

230   of the effects (**Fig. 4c**). Toward this end, these results highlight that leucine zipper-based SAIM imaging can serve

231   as a powerful screening tool for evaluating the effects of inhibitors and enzymatic degraders on the glycocalyx layer.

232   **Ac$_5$GalNTGc enhances immune cell cytotoxicity by reducing glycocalyx thickness**

233   To investigate whether the reduction in glycocalyx thickness by Ac$_5$GalNTGc corresponds with enhanced immune

234   cell recognition and killing, we utilized a previously validated cellular model with readily tunable MUC1 expression

235   via doxycycline-induced expression, referred to here as 1E7[13]. The green fluorescent protein, mOxGFP, was

236   genetically inserted between the ectodomain and transmembrane domain of MUC1, enabling the visualization of

237   cell-surface MUC1 and quantification of its expression level. Using this cellular model system, we first confirmed

238   that the cell-surface MUC1 level of YSCCC is similar to the 1E7 clone. (**Fig. 5a**). We next used 1E7 cells to examine

239   how Ac$_5$GalNTGc affects glycosylation of the MUC1 ectodomain displayed on the cell surface. Treatment of 1E7

240   cells with 100 µM Ac$_5$GalNTGc resulted in decreased cell-surface expression of both MUC1-GFP and core-1

241   glycans, as measured by GFP signal and PNA lectin labeling, respectively (**Fig. 5b,c**). SAIM analysis revealed that

242   higher induction of MUC1-GFP led to a substantial reduction in glycocalyx thickness following Ac$_5$GalNTGc

243   treatment compared to wild-type 1E7 cells (**Fig. 5d**). This effect was most pronounced at maximum doxycycline

244   induction, where Ac$_5$GalNTGc treatment reduced glycocalyx thickness by 13.9 nm relative to wild-type cells (**Fig.**

245   **5d**). These results align with our previous findings demonstrating the impact of O-glycosylation on glycocalyx

246   thickness[13]. We then confirmed that protection against NK-92 cell-mediated killing depended on the glycocalyx

247   thickness of the target cells. Remarkably, we observed a significant increase in NK-92 cell-mediated cytotoxicity

248   against Ac$_5$GalNTGc-treated cells compared to wild-type 1E7 cells (**Fig. 5e**). Consistent with the inverse correlation

249   observed in our previous study[13], these results further demonstrate an inverse relationship between glycocalyx

250   thickness and NK-92 cell-mediated cytotoxicity following treatment with Ac$_5$GalNTGc (**Fig. 5f**). To extend these

251   findings to engineered immune cells, we investigated whether Ac$_5$GalNTGc treatment could enhance CD19-

252   targeted chimeric antigen receptor NK (CD19 CAR-NK) cell efficacy (**Fig. 5g**). Using 1E7 cells engineered to

253   overexpress CD19, we observed a remarkable 3.02-fold increase in CD19 CAR-NK cell-mediated cytotoxicity

254   following Ac$_5$GalNTGc treatment (**Fig. 5g**). These results demonstrate that pharmacological reduction of

255   glycocalyx thickness can significantly enhance both natural and engineered immune cell responses, suggesting

256   potential therapeutic applications in cancer immunotherapy.

257

Safety evaluation and anti-tumor efficacy of StcE-NK cells in YSCCC xenograft model

In addition to $Ac_5GalNTGc$, enzymatic mucin degraders showed potential as agents to compromise the integrity of the CCA glycocalyx (**Fig. 3c-j**). However, severe adverse effects have been observed in rodent models following systemic injection with StcE[11]. To overcome this safety issue, work from our group has proposed that immune cells could be engineered to deliver enzymes locally to target cancer cells, thus, lowering the total enzyme dosage that would be required for anti-tumor functionality[13]. In one implementation of this strategy, StcE mucinases were coupled to the surface of NK cells utilizing the same leucine zipper pairs presented in this study for membrane labelling[13] (**Fig. 6a**). Employing this strategy here, *in vitro* cytotoxicity assays demonstrated that StcE-tethered NK cells exhibited 2.9-fold enhanced killing activity against YSCCC cells compared to unmodified NK cells (**Fig. 6b**).

Given these promising results, we tested the safety and functionality of the StcE-NK cells *in vivo*. To assess the safety profile of StcE-NK cells, we conducted toxicity studies in immunocompromised NSG mice using the maximum therapeutic dose of 10×10^6 cells administered via intraperitoneal (IP) injection (**Fig. 6c**). Body weight monitoring over 25 days revealed no significant toxicity across all NK cell treatment groups, including the StcE-NK cohort (**Fig. 6d**). Comprehensive histopathological evaluation of major organs (liver, spleen, kidney, small intestine, pancreas, heart, gallbladder, lung, brain, stomach, and esophagus) by an expert pathologist revealed no histological abnormalities. These findings confirm both the suitability of the YSCCC dose for consistent tumor establishment and the favorable safety profile of StcE-NK cells in NSG mice.

To validate these findings *in vivo*, we established a new YSCCC mouse xenograft model. Immunocompromised NSG mice received 5×10^6 YSCCC cells via either IP or subcutaneous (SubQ) injection routes (**Fig. 6e**). Our experiments demonstrated robust engraftment and tumor growth following SubQ implantation (**Fig. 6f,g**). Engraftment as assessed by magnetic resonance imaging (MRI) was not observed in the IP model. Therefore, to evaluate therapeutic efficacy *in vivo*, we established SubQ YSCCC xenografts by injecting 5×10^6 YSCCC cells into NSG mice. Once tumors reached an average volume of 150-250 mm³, we initiated treatment with intratumoral injections of 3×10^6 wild-type or StcE-NK cells. Treatment was administered weekly for three consecutive weeks, and tumor progression was monitored via caliper measurements over a 53-day period (**Fig. 6h**). Consistent with our

283   *in vitro* result in **Fig. 6a**, StcE-NK cells demonstrated significantly enhanced anti-tumor activity compared to both

284   wild-type NK cells and PBS control groups (**Fig. 6i,j**). Importantly, no treatment-related toxicity was observed

285   throughout the study period, as evidenced by stable body weights and normal behavioral patterns across all

286   treatment groups (**Fig. 6k**). These results validate the therapeutic potential of StcE-NK cells against MUC1-

287   overexpressing CCA *in vivo*.

288

Discussion

290   In this study, we developed a novel membrane fluorescent labeling approach by combining leucine-zipper pairs and

291   sortase-mediated reactions to overcome critical limitations of conventional methods, such as poor membrane

292   retention and non-specific labeling. We further combined this labeling strategy with SAIM imaging to precisely

293   quantify cancer cell glycocalyx thickness with nanoscale resolution. We used this platform to identify the small-

294   molecule $Ac_5GalNTGc$ and StcE mucinase as potent agents to reduce glycocalyx thickness in multiple MUC1-

295   overexpressing cancer cell lines, such as YSCCC and KPL-1. We further validated that StcE treatment can reverse

296   the physical effects of the repulsive mucin barrier on YSCCC cells in cell-substrate and cell-cell adhesion assays.

297   Based on these mechanistic insights, we validated a therapeutic approach using StcE-tethered NK cells, which

298   effectively penetrated the mucin barrier and demonstrated significant anti-tumor activity in a xenograft model,

299   establishing a promising strategy for targeting mucin-overexpressing cancers. These findings establish our imaging

300   platform as a valuable tool for screening glycocalyx-modifying compounds and validate glycocalyx reduction as a

301   promising strategy for improving immunotherapy efficacy.

302   Our leucine zipper-based labeling strategy, while enabling glycocalyx measurements across diverse cancer types,

303   has certain limitations. A key technical constraint is the requirement for Bzip overexpression in target cells through

304   genetic modification. Although our analyses revealed that Bzip expression does not significantly alter cell viability

305   or morphology, comprehensive characterization of its potential effects on membrane properties is pending. Future

306   studies should specifically investigate how Bzip expression might influence adhesion molecule dynamics,

307   membrane fluctuations, and nanoscale organization of cell surface components. Additionally, while beyond the

308 scope of the current study, the development of orthogonal leucine zipper labeling approaches could provide

309 complementary insights into membrane protein interactions and dynamics[45]. Such multi-modal analyses would

310 further enhance our understanding of the complex interplay between glycocalyx structure and membrane

311 organization in cancer cells.

312 The robustness of our system across different cancer cell types also enabled the observation of distinct patterns of

313 glycocalyx regulation across different cancer types. KPL-1 breast cancer cells showed remarkable sensitivity to

314 sialylation inhibition, with P-3F$_{AX}$-Neu5Ac treatment reducing glycocalyx thickness by an average of 40 nm. In

315 contrast, YSCCC intrahepatic CCA cells demonstrated more significant response to O-GalNAc modification

316 through Ac$_5$GalNTGc treatment. These differential responses suggest that cancer cells may develop specific

317 dependencies on particular glycosylation pathways, potentially reflecting their tissue of origin or malignant

318 adaptation[46]. Understanding these cell type-specific dependencies could inform the design of more refined targeted

319 therapeutic strategies.

320 While MUC1-targeted immunotherapy continues to evolve, clinically significant results remain elusive[47,48]. Our

321 approach differs fundamentally from conventional CAR-T or CAR-NK strategies by directly addressing the mucin

322 barrier that impedes immune cell recognition. By employing the StcE enzyme to breach this barrier, we enhance

323 immune cell recognition and targeting efficiency. This strategy holds potential for combination with various

324 immunotherapeutic approaches, including CAR-T cells, although further investigation of StcE-NK cell mechanisms

325 is necessary. While our current study demonstrated efficacy through intratumoral injection, future research should

326 explore alternative administration routes, particularly intravenous delivery, to optimize therapeutic applications.

327 Our findings have important implications for clinical translation. The differential glycocalyx regulation patterns we

328 observed across cancer types suggest the need for personalized approaches to glycocalyx-targeting therapies.

329 Moreover, our platform provides a valuable tool for patient stratification and monitoring treatment response. While

330 our study demonstrates the potential of glycocalyx-targeting approaches, several limitations should be addressed in

331 future work. These include the need for long-term safety studies of StcE-NK cells, optimization of delivery methods,

332 and investigation of potential resistance mechanisms. Future studies should focus on several key areas, such as

333   optimization of StcE-NK cell delivery methods for systemic administration and investigation of potential

334   combination strategies with existing immunotherapies.

335

Materials and methods

337   **Cell culture**

338   MCF10A cells were cultured in DMEM/F12 media (Thermo Fisher Scientific) supplemented with 5% horse serum

339   (Thermo Fisher Scientific), 20 ng/ml EGF (Pepro Tech), 10 mg/ml insulin (Sigma), 500 ng/ml hydrocortisone

340   (Sigma), 100 ng/ml cholera toxin (Sigma) and 1x penicillin/streptomycin (Thermo Fisher Scientific) at 37°C in 5%

341   CO_2. HEK293T cells (gift from Valerie Weaver) were cultured in DMEM high glucose media (Thermo Fisher

342   Scientific) supplemented with 10% fetal bovine serum (Thermo Fisher Scientific) and 1x penicillin/streptomycin at

343   37°C in 5% CO_2. YSCCC (RIKEN BRC; RCB1549), ZR-75-1 (ATCC; CRL-1500), T47D (ATCC; HTB-133),

344   SKBR3 (gift from Dr. Jan Lammerding), KPL-1 (DSMZ; ACC 317), and Capan-2 (ATCC; HTB-80) cells were

345   cultured in RPMI 1640 media (Thermo Fisher Scientific) supplemented with 10% fetal bovine serum and 1x

346   penicillin/streptomycin at 37°C in 5% CO_2. NK-92 cells (ATCC; CRL-2407) were cultured in α-MEM without

347   ribonucleosides media (Thermo Fisher Scientific) supplemented with 12.5% fetal bovine serum, 12.5% horse serum,

348   0.2 mM Myo-inositol (Sigma Aldrich), 0.1 mM 2-mercaptoethanol (Thermo Fisher Scientific), 0.02 mM folic acid

349   (Millipore Sigma), 100 U/ml recombinant human IL-2 (Pepro Tech), and 1x penicillin/streptomycin at 37°C in 5%

350   CO_2.

351   **Immunostaining and live cell imaging**

352   Target cells were plated in 35-mm glass-bottom dishes and cultured for 24 hours. For standard conditions, cells

353   were labeled with 1 µM Azip-based dyes (Azip-sfGFP, Azip-AF488, or Azip-AF647) in phenol red-free culture

354   media for 10 minutes at 37°C. For cold conditions, cells were labeled with 1 µM Azip-based dyes in 0.5% BSA

355   PBS for 1 hour at 4°C. For 48-hour live cell imaging experiments, cells were labeled according to manufacturers'

356   recommended buffer compositions and concentrations for 10 minutes at 37°C. Before imaging, cells were washed

357   twice with either cold PBS or phenol red-free culture media. All samples were imaged at 0, 4, 24, and 48 hours at

358   37°C under 5% CO2.

359   For live cell imaging of 1E7 cells in response to inhibitors, cells were first induced with various concentrations of

360   doxycycline for 24 hours, then treated with either DMSO or 100 μM Ac$_5$GalNTGc for 48 hours. All imaging was

361   performed using an LSM 800 confocal microscope with either a ×20 air objective (NA 0.8) or ×63 water objective

362   (NA 1.2) (ZEISS). ImageJ was used for image analysis.

363   **Flow cytometry**

364   To measure cell surface Muc1 expression in cancer cell lines, cells were plated, grown for at least 48 hours, and

365   detached using trypsin. Anti-Muc1 antibody clone HMPV (555925, BD Biosciences) was diluted 1:200 in 0.5%

366   w/v BSA in 1x PBS and incubated with the cells at 4°C for 1 hour. Secondary labelling was with Alexa Fluor 647

367   conjugated goat anti-mouse, diluted 1:200 in 0.5% w/v BSA in PBS and incubated with cells at 4°C for 1 hour. In

368   each experiment, SKBR3 cells were included as a standard for comparison. Median fluorescence intensity was

369   calculated in FlowJo and values were normalized to the median fluorescence intensity of SKBR3 cells in each

370   experiment. For lectin staining, detached target cancer cells were incubated with PNA-CF650R at 4°C for 1 hour.

371   Lectin was diluted 1:200 in 0.5% BSA PBS and incubated with cells at 4°C for 1 hour. The Attune NxT flow

372   cytometry (Thermo Fisher Scientific) was used for analysis.

373   **Sortase-mediated labeling reaction**

374   100 μM Azip-LPETG-sfGFP was incubated in reaction buffer (50 mM Tris-HCl, pH 7.5, 150 mM NaCl, 10 mM

375   CaCl2) containing 20 μM sortase and 10 mM triglycine (Gly$_3$)-conjugated AF488 or AF647. After 1-3 hours of

376   incubation at room temperature, the reaction products were purified using HisPur Ni-NTA Resin to remove

377   unreacted His6-tagged Azip dye and His6-tagged Sortase in elution buffer (20 mM HEPES, 500 mM NaCl, 10 mM

378   imidazole, pH 7.5). The column flow-through was then buffer-exchanged to PBS to remove unbound dye.

NK-92 cell-mediated cytotoxicity assays

Target cells were detached and fluorescently labeled for 15 minutes with 10 μM CellTracker Green CMFDA Dye (Invitrogen) in growth media, followed by washing thoroughly twice with growth media. 4×10^4 labeled target cells were mixed with varying ratios of NK-92 cells in 200 μL of growth media of the target cell line in the absence of IL-2 and co-cultured in an ultra-low attachment U-bottom 96-well plate (Corning) for 4 hours at 37°C in 5% CO_2. Following the 4-hour co-culture, the mixed cells were pelleted by centrifugation at 500 g for 5 minutes, resuspended and incubated in propidium iodide solution (PI; 20 μg/mL, Sigma) for 10 minutes. NK cell-mediated cytotoxicity was then measured by flow cytometry as previously described[7,13,49]. At least 1×10^4 tumor cells were analyzed after electronic gating on CellTracker Green. To calculate the percent cytotoxicity, the following formula was used: 100 × (experimental % dead − spontaneous % dead)/(100 − spontaneous % dead), where experimental % dead was the percentage of PI positive tumor cells in co-cultures and spontaneous % dead was the percentage of PI positive control tumor cells cultured in the absence of effector cells.

Scanning angle interference microscopy (SAIM)

Silicon wafers with a ~2,000 nm thermal oxide layer (Addison Engineering) were diced into 7 × 7 mm chips, and the oxide layer thickness of each chip was measured with a FilMetrics F50-EXR. Silicon chips then were functionalized using 4% (v/v) (3-mercaptopropyl)trimethoxysilane in absolute ethanol for 30 minutes at room temperature, followed by incubation with 4 mM 4-maleimidobutyric acid N-hydroxysuccinimide ester in absolute ethanol and 50 μg/ml human Alexa Fluor 647 conjugated plasma fibronectin as previously reported[13,50]. Cells were seeded onto the fibronectin-coated chips at $0.5-1 \times 10^5$ cells/cm² in full culture medium. After 24 hours, adhered cells were rinsed with phenol-red free RPMI and incubated with Azip-AF488 in phenol-red free RPMI for 10 minutes at 37°C. For SAIM imaging of 1E7 cells, cells were induced with various doxycycline concentrations for 24 hours and then rinsed with serum-free, phenol-red free DMEM and incubated with MemGlow dyes (MemGlow 560, MG02-2; Cytoskeleton) in serum-free, phenol red-free DMEM for 10 minutes at 37°C. Cell-seeded chips were then washed with serum-free, phenol red-free DMEM or phenol red-free RPMI again, and inverted onto a 35 mm

403 glass-bottom imaging dish and imaged at 37°C. As previously reported[13], SAIM was conducted on a custom circle-

404 scanning microscope which allowed imaging at varying incidence angles, ranging from 5 to 43.75 degrees, and a

405 total of 32 images was acquired per cell. The intensities of raw image sequences were fit pixelwise by nonlinear

406 least-squares to an optical model:

407
$$I_j = A * f(\theta_j, H) + B$$

408 where I_j is raw image intensity at each incidence angle θ_j, H is the glycocalyx thickness, and A and B are additional

409 fit parameters. The optical system maintained the s-polarization of circle-scanned excitation laser by the vortex

410 half-wave plate. The probability of excitation is given by:

411
$$f(\theta_j, H) = 1 + 2Re\{r^{TE}\}\cos\phi - 2Im\{r^{TE}\}\sin\phi + Re\{r^{TE}\}^2 + Im\{r^{TE}\}^2$$

412 Where $\phi(H)$ is the phase shift, λ is s-polarized monochromatic excitation of wavelength, and r^{TE} is the reflection

413 coefficient for the transverse electric wave and these are given by:

414
$$\phi(H) = \frac{4\pi}{\lambda}(n_b H \cos\theta_b)$$

415
$$r^{TE} = \frac{(m_{11}^{TE} + m_{12}^{TE} p_{Si})p_2 - (m_{21}^{TE} + m_{22}^{TE} p_0)}{(m_{11}^{TE} + m_{12}^{TE} p_{Si})p_2 + (m_{21}^{TE} + m_{22}^{TE} p_0)}$$

416
$$M^{TE} = \begin{pmatrix} m_{11}^{TE} & m_{12}^{TE} \\ m_{21}^{TE} & m_{22}^{TE} \end{pmatrix} = \begin{pmatrix} \cos(k_{ox}d_{ox}\cos\theta_{ox}) & -\frac{i}{p_1}\sin(k_{ox}d_{ox}\cos\theta_{ox}) \\ -ip_1\sin(k_{ox}d_{ox}\cos\theta_{ox}) & \cos(k_{ox}d_{ox}\cos\theta_{ox}) \end{pmatrix}$$

417
$$p_0 = n_{Si}\cos\theta_{Si}, p_1 = n_{ox}\cos\theta_{ox}, p_2 = n_b\cos\theta_b$$

418
$$k_i = \frac{2\pi n_i}{\lambda}, \theta_{ox} = \sin^{-1}\frac{n\sin\theta_b}{n_{ox}}, \theta_{Si} = \sin^{-1}\frac{n\sin\theta_{ox}}{n_{Si}}$$

419 where k_i is the wavenumber in material i; n_{Si}, n_{ox} and n_b are the refractive index of the silicon, silicon oxide and

420 sample, respectively; θ_{Si}, θ_{ox} and θ_b are the angles of incidence in the silicon, silicon oxide and sample,

421 respectively; and d_{ox} is the thickness of the silicon oxide layer. The angles of incidence in silicon oxide and silicon

422 were calculated according to Snell's Law. The average glycocalyx thickness was quantified in 200×200 pixel

423 subregions of each cell by subtracting the height of their MemGlow signal or Azip signal from the height of the

424 corresponding fluorescently labeled fibronectin on the silicon substrate.

425 **Preparation of recombinant StcE and SmE mucinases**

426 The cDNA for StcE-Δ35 and SmE was synthesized by custom gene synthesis (Twist Bioscience) and inserted into

427 the pET28b expression vector[37]. The recombinant enzymes were produced by expressing them in chemically

428 competent NiCo21 (DE3) E. coli (NEB). Following transformation and overnight growth on Luria Broth (LB) agar

429 plates, the cells were cultured in LB medium at 37°C until an OD600 of 0.6-0.8 was reached. At this point, the

430 cultures were induced with 0.5 mM isopropyl β-D-1-thiogalactopyranoside (IPTG) and grown overnight at 24°C.

431 Cells were then harvested by centrifugation at 3,000 g for 20 minutes, resuspended in lysis buffer (20 mM HEPES,

432 500 mM NaCl and 10 mM imidazole, pH 7.5) with cOmplete protease inhibitor Cocktail (Roche), and lysed by a

433 sonicator (Q125, Qsonica). Recombinant enzymes were purified by immobilized metal affinity chromatography

434 (IMAC) on a GE ÄKTA Avant FPLC system. The lysate was applied to a HisTrap HP column (Cytiva), followed

435 by a wash step with 20 column volumes of wash buffer (20 mM HEPES, 500 mM NaCl and 20 mM imidazole, pH

436 7.5). Elution was performed using a linear gradient of 20 mM to 250 mM imidazole in buffer (20 mM HEPES and

437 500 mM NaCl, pH 7.5). The eluted fractions containing target protein were collected and further refined by a HiPrep

438 26/60 Sephacryl S-200 HR (Cytiva) column equilibrated with storage buffer (20 mM HEPES and 150 mM NaCl,

439 pH 7.5). The final protein was concentrated by using Amicon Ultra 30 kDa MWCO filters (Millipore Sigma).

440 **Assessment of cell-substrate adhesion**

441 YSCCC cells were plated at 80,000 cells per well in a 24-well plate (Cellstar, #662160) in RPMI 1640 media with

442 10% fetal bovine serum and 1% penicillin/streptomycin. Where specified, StcE or SmE mucinases were added to a

443 final concentration of 1 nM. Cells were allowed to adhere to the plates for 18 hours in 37°C and 5% CO_2. Phase

444 contrast images were then acquired on a BZ-X810 fluorescence box microscope (Keyence) using a 20x (NA: 0.45)

445   air objective. Cells were manually segmented and counted in ImageJ to calculate circularity and fraction of rounded

446   cells (cells with a Circularity > 0.9). Rounded cell fraction was calculated as (# rounded cells)/(# rounded cells + #

447   spread cells) in each field of view.

Assessment of cell-cell adhesion

449   YSCCC cells were detached with 0.25% trypsin. Cells were seeded at 1,000 cells per well in 150 uL 96-well ultra-

450   low adhesion plates (Corning #7007) in the presence of 0.05% methylcellulose (M6385, Millipore Sigma). Where

451   specified, StcE was added to a final concentration of 10 nM. The plate was then gently centrifuged at 150xg for 3

452   minutes to ensure that all cells collected at the bottom of each well. Cells were then allowed to form aggregates for

453   24 hours at 37°C and 5% CO_2. Cell aggregates were then imaged on an LSM 800 confocal microscope using the

454   brightfield mode with a 10x (NA: 0.3 Air) objective. Aggregates were then manually segmented in ImageJ to

455   calculate overall aggregate area.

Mouse Xenograft Model

457   Male 8-10 week-old in-house bred NOD.Cg-Prkdcscid Il2rgtm1Wjl/SzJ (NSG) mice (The Jackson Laboratory

458   Catalog #005557) were housed in groups of up to five under pathogen-free conditions. The animals were kept at

459   temperatures of 21.1-24.5°C (70-76°F), 30-70% humidity, and a 12:12 light-dark cycle. All mice were housed at

460   the East Campus Research Facility (ECRF) at Cornell University and all care and experiments were conducted in

461   accordance with protocols approved by the Cornell University Institutional Animal Care and Use Committee under

462   protocol number 2017-0035. Cell line derived xenograft (CDX) mice (n = 20) were established by injecting cultured

463   YSCCC cells at a titer of $5x10^6$ cells per 100uL and with 100uL of Corning Matrigel into the left rear flank of NSG

464   mice while under 2.5% isoflurane anesthesia. Mice were monitored twice per week for tumor growth using digital

465   calipers. Once tumor burden reached start criteria of 150-200mm³ mice were randomly sorted into one of three

466   treatment groups: StcE-tethered NK-92, wild-type NK-92, or PBS (n = 5/group). Mice were intratumorally injected

467   with treatment compounds using a 28G BD Insulin Syringe (Catalog# 329461) once per week for three weeks. Body

468   weight and caliper measurements were taken twice per week while on treatment. At the end of the experiment mice

469 were sacrificed using CO_2 euthanasia and tumors were excised from the animals and placed in 10% neutral buffered

470 formalin for further histological analysis.

Statistical analysis

472 Unless otherwise indicated, results are presented as the mean and standard deviation (s.d.) of at least three replicates

473 per condition using GraphPad Prism 9. Statistical differences were determined using a two-tailed unpaired t-test for

474 two group comparisons, one-way ANOVA with multiplicity-adjusted p values from Tukey's multiple comparisons

475 test, and two-way ANOVA with correction for multiple comparisons. Statistical significance was determined using

476 two-tailed unpaired t-tests, one-way ANOVA, and two-way ANOVA, with $p < 0.05$ considered significant across

477 all analyses.

Acknowledgments

Author contributions

488 S.P., J.H.P, and M.J.P. designed the project. S.P. conducted the SAIM measurements and analysis. S.P., and J.H.P.,

489 conducted and analyzed all cytotoxicity assay and flow cytometry. S.P., J.H.P., and M.J.P. wrote the manuscript with

490 feedback from all authors.

Author Information

Matthew J. Paszek (mjp31@cornell.edu)

Address: 120 Olin Hall, 113 Ho Plaza, Cornell University, Ithaca NY 14853, USA

Conflicts of Interest

M.J.P. and S.P are inventors on a patent filed by Cornell's Center for Technology Licensing on the StcE-tethered NK technology (PCT/US2022/080937). All other authors declare no competing interests.

References

1. Kuo, J. C.-H., Gandhi, J. G., Zia, R. N. & Paszek, M. J. Physical biology of the cancer cell glycocalyx. *Nature Phys* **14**, 658–669 (2018).

2. Burchell, J. M., Beatson, R., Graham, R., Taylor-Papadimitriou, J. & Tajadura-Ortega, V. O-linked mucin-type glycosylation in breast cancer. *Biochem Soc Trans* **46**, 779–788 (2018).

3. Gupta, R., Leon, F., Rauth, S., Batra, S. K. & Ponnusamy, M. P. A Systematic Review on the Implications of O-linked Glycan Branching and Truncating Enzymes on Cancer Progression and Metastasis. *Cells* **9**, E446 (2020).

4. Mereiter, S., Balmaña, M., Campos, D., Gomes, J. & Reis, C. A. Glycosylation in the Era of Cancer-Targeted Therapy: Where Are We Heading? *Cancer Cell* **36**, 6–16 (2019).

5. RodrÍguez, E., Schetters, S. T. T. & van Kooyk, Y. The tumour glyco-code as a novel immune checkpoint for immunotherapy. *Nat Rev Immunol* **18**, 204–211 (2018).

6. van de Wall, S., Santegoets, K. C. M., van Houtum, E. J. H., Büll, C. & Adema, G. J. Sialoglycans and Siglecs Can Shape the Tumor Immune Microenvironment. *Trends Immunol* **41**, 274–285 (2020).

7. Hudak, J. E., Canham, S. M. & Bertozzi, C. R. Glycocalyx engineering reveals a Siglec-based mechanism for NK cell immunoevasion. *Nat Chem Biol* **10**, 69–75 (2014).

8. Perdicchio, M. *et al.* Sialic acid-modified antigens impose tolerance via inhibition of T-cell proliferation and de novo induction of regulatory T cells. *Proc Natl Acad Sci U S A* **113**, 3329–3334 (2016).

515   9.   Kantarjian, H. M. *et al.* Inotuzumab Ozogamicin versus Standard Therapy for Acute Lymphoblastic

516   Leukemia. *N Engl J Med* **375**, 740–753 (2016).

517   10. Walter, R. B. Investigational CD33-targeted therapeutics for acute myeloid leukemia. *Expert Opin Investig*

518   *Drugs* **27**, 339–348 (2018).

519   11. Pedram, K. *et al.* Design of a mucin-selective protease for targeted degradation of cancer-associated mucins.

520   *Nat Biotechnol* (2023) doi:10.1038/s41587-023-01840-6.

521   12. Stark, J. C. *et al.* Antibody-lectin chimeras for glyco-immune checkpoint blockade. Preprint at

522   https://doi.org/10.1101/2022.10.26.513931 (2022).

523   13. Park, S. *et al.* Immunoengineering can overcome the glycocalyx armour of cancer cells. *Nat. Mater.* **23**, 429–

524   438 (2024).

525   14. Brindley, P. J. *et al.* Cholangiocarcinoma. *Nat Rev Dis Primers* **7**, 65 (2021).

526   15. Park, S. Y. *et al.* Expression of MUC1, MUC2, MUC5AC and MUC6 in cholangiocarcinoma: prognostic

527   impact. *Oncol Rep* **22**, 649–657 (2009).

528   16. Ilyas, S. I. *et al.* Cholangiocarcinoma - novel biological insights and therapeutic strategies. *Nat Rev Clin*

529   *Oncol* **20**, 470–486 (2023).

530   17. Greten, T. F. *et al.* Immunology and immunotherapy of cholangiocarcinoma. *Nat Rev Gastroenterol Hepatol*

531   **20**, 349–365 (2023).

532   18. Möckl, L. *et al.* Quantitative Super-Resolution Microscopy of the Mammalian Glycocalyx. *Developmental*

533   *Cell* **50**, 57-72.e6 (2019).

534   19. Lelek, M. *et al.* Single-molecule localization microscopy. *Nat Rev Methods Primers* **1**, 39 (2021).

535   20. Choy, E. *et al.* Endomembrane trafficking of ras: the CAAX motif targets proteins to the ER and Golgi. *Cell*

536   **98**, 69–80 (1999).

537   21. Lubart, Q. *et al.* Lipid vesicle composition influences the incorporation and fluorescence properties of the

538   lipophilic sulphonated carbocyanine dye SP-DiO. *Phys Chem Chem Phys* **22**, 8781–8790 (2020).

539   22. Zhanghao, K. *et al.* High-dimensional super-resolution imaging reveals heterogeneity and dynamics of

540   subcellular lipid membranes. *Nat Commun* **11**, 5890 (2020).

541   23. Paszek, M. J. *et al.* Scanning angle interference microscopy reveals cell dynamics at the nanoscale. *Nature*
542   *Methods* **9**, 825–827 (2012).

543   24. Son, S. *et al.* Molecular height measurement by cell surface optical profilometry (CSOP). *Proc Natl Acad Sci*
544   *U S A* **117**, 14209–14219 (2020).

545   25. Ajo-Franklin, C. M., Ganesan, P. V. & Boxer, S. G. Variable Incidence Angle Fluorescence Interference
546   Contrast Microscopy for Z-Imaging Single Objects. *Biophysical Journal* **89**, 2759–2769 (2005).

547   26. Colville, M. J., Park, S., Zipfel, W. R. & Paszek, M. J. High-speed device synchronization in optical
548   microscopy with an open-source hardware control platform. *bioRxiv* 533349 (2019) doi:10.1101/533349.

549   27. Cho, J. H., Collins, J. J. & Wong, W. W. Universal Chimeric Antigen Receptors for Multiplexed and Logical
550   Control of T Cell Responses. *Cell* **173**, 1426-1438.e11 (2018).

551   28. Reinke, A. W., Grant, R. A. & Keating, A. E. A synthetic coiled-coil interactome provides heterospecific
552   modules for molecular engineering. *J Am Chem Soc* **132**, 6025–6031 (2010).

553   29. Thompson, K. E., Bashor, C. J., Lim, W. A. & Keating, A. E. SYNZIP protein interaction toolbox: in vitro
554   and in vivo specifications of heterospecific coiled-coil interaction domains. *ACS Synth Biol* **1**, 118–129
555   (2012).

556   30. Collot, M. *et al.* MemBright: A Family of Fluorescent Membrane Probes for Advanced Cellular Imaging and
557   Neuroscience. *Cell Chem Biol* **26**, 600-614.e7 (2019).

558   31. Shurer, C. R. *et al.* Genetically Encoded Toolbox for Glycocalyx Engineering: Tunable Control of Cell
559   Adhesion, Survival, and Cancer Cell Behaviors. *ACS Biomater. Sci. Eng.* **4**, 388–399 (2018).

560   32. Paszek, M. J. *et al.* The cancer glycocalyx mechanically primes integrin-mediated growth and survival.
561   *Nature* **511**, 319–325 (2014).

562   33. Chongsaritsinsuk, J. *et al.* Glycoproteomic landscape and structural dynamics of TIM family immune
563   checkpoints enabled by mucinase SmE. *Nat Commun* **14**, 6169 (2023).

564   34. Malaker, S. A. *et al.* The mucin-selective protease StcE enables molecular and functional analysis of human
565   cancer-associated mucins. *Proc. Natl. Acad. Sci. U.S.A.* **116**, 7278–7287 (2019).

566   35. Yu, A. C. Y., Worrall, L. J. & Strynadka, N. C. J. Structural Insight into the Bacterial Mucinase StcE Essential

567   to Adhesion and Immune Evasion during Enterohemorrhagic E. coli Infection. *Structure* **20**, 707–717 (2012).

568   36. Shurer, C. R., Head, S. E., Goudge, M. C. & Paszek, M. J. Mucin-coating technologies for protection and

569   reduced aggregation of cellular production systems. *Biotechnology and Bioengineering* **116**, 994–1005

570   (2019).

571   37. Yuan, Y., Wu, L., Shen, S., Wu, S. & Burdick, M. M. Effect of alpha 2,6 sialylation on integrin-mediated

572   adhesion of breast cancer cells to fibronectin and collagen IV. *Life Sci* **149**, 138–145 (2016).

573   38. Suzuki, O., Abe, M. & Hashimoto, Y. Sialylation and glycosylation modulate cell adhesion and invasion to

574   extracellular matrix in human malignant lymphoma: Dependency on integrin and the Rho GTPase family. *Int*

575   *J Oncol* **47**, 2091–2099 (2015).

576   39. Agarwal, K. *et al.* Inhibition of Mucin-Type *O* -Glycosylation through Metabolic Processing and

577   Incorporation of *N* -Thioglycolyl- D -galactosamine Peracetate (Ac $_5$ GalNTGc). *J. Am. Chem. Soc.* **135**,

578   14189–14197 (2013).

579   40. Wang, S.-S. *et al.* Efficient inhibition of O-glycan biosynthesis using the hexosamine analog Ac5GalNTGc.

580   *Cell Chemical Biology* **28**, 699-710.e5 (2021).

581   41. Dwivedi, V., Saini, P., Tasneem, A., Agarwal, K. & Sampathkumar, S.-G. Differential inhibition of mucin-

582   type O-glycosylation (MTOG) induced by peracetyl N-thioglycolyl-d-galactosamine (Ac5GalNTGc) in

583   myeloid cells. *Biochemical and Biophysical Research Communications* **506**, 60–65 (2018).

584   42. Rillahan, C. D. *et al.* Global metabolic inhibitors of sialyl- and fucosyltransferases remodel the glycome. *Nat*

585   *Chem Biol* **8**, 661–668 (2012).

586   43. Büll, C. *et al.* Targeting Aberrant Sialylation in Cancer Cells Using a Fluorinated Sialic Acid Analog Impairs

587   Adhesion, Migration, and *In Vivo* Tumor Growth. *Molecular Cancer Therapeutics* **12**, 1935–1946 (2013).

588   44. Huang, Y.-F. *et al.* Global mapping of glycosylation pathways in human-derived cells. *Dev Cell* **56**, 1195-

589   1209.e7 (2021).

590   45. Lebar, T., Lainšček, D., Merljak, E., Aupič, J. & Jerala, R. A tunable orthogonal coiled-coil interaction

591   toolbox for engineering mammalian cells. *Nat Chem Biol* **16**, 513–519 (2020).

592   46. Reily, C., Stewart, T. J., Renfrow, M. B. & Novak, J. Glycosylation in health and disease. *Nat Rev Nephrol*

593   **15**, 346–366 (2019).

594   47. Tong, X., Dong, C. & Liang, S. Mucin1 as a potential molecule for cancer immunotherapy and targeted

595   therapy. *J Cancer* **15**, 54–67 (2024).

596   48. Ibrahim, N. K. *et al.* Randomized phase II trial of letrozole plus anti-MUC1 antibody AS1402 in hormone

597   receptor-positive locally advanced or metastatic breast cancer. *Clin Cancer Res* **17**, 6822–6830 (2011).

598   49. Bryceson, Y. T. *et al.* Functional analysis of human NK cells by flow cytometry. *Methods Mol Biol* **612**, 335–

599   352 (2010).

600   50. Colville, M., Park, S., Singh, A., Paszek, M. & Zipfel, W. R. Azimuthal Beam Scanning Microscope Design

601   and Implementation for Axial Localization with Scanning Angle Interference Microscopy. in *Biomedical*

602   *Engineering Technologies* (eds. Ossandon, M. R., Baker, H. & Rasooly, A.) vol. 2393 127–152 (Springer US,

603   New York, NY, 2022).

604   51. Yu, A. C. Y., Worrall, L. J. & Strynadka, N. C. J. Structural Insight into the Bacterial Mucinase StcE Essential

605   to Adhesion and Immune Evasion during Enterohemorrhagic E . coli Infection. *Structure* **20**, 707–717 (2012).
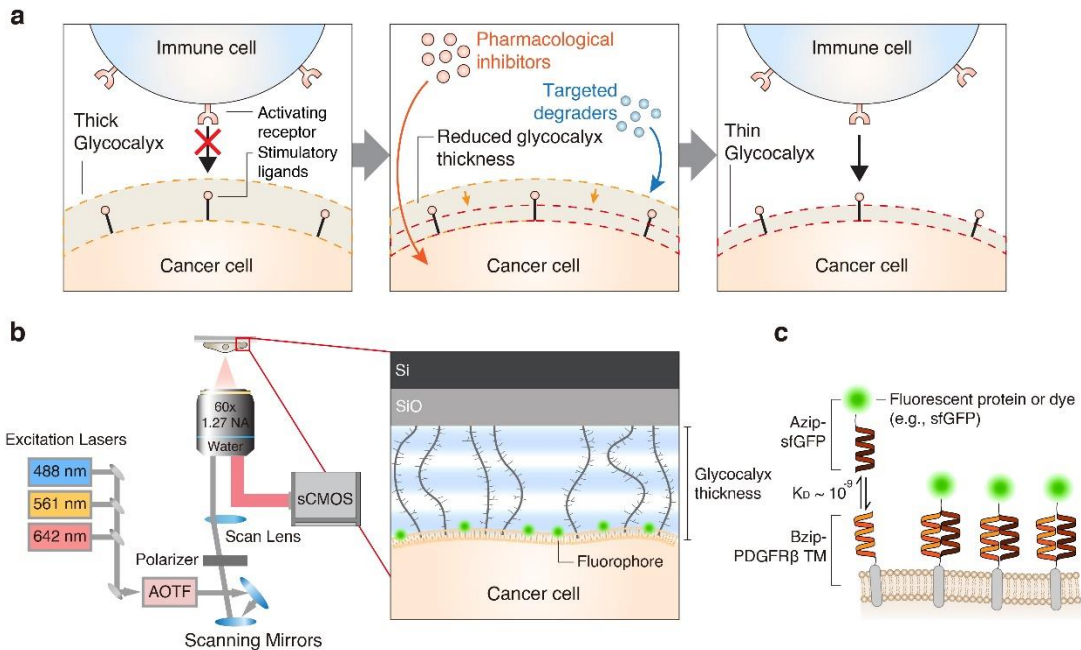
606

Figure 1: SAIM illustration and potential use for drug screening. a, Schematic representation of cellular glycocalyx thickness changes induced by pharmacological inhibitors or targeted degraders to enhance immune cell recognition. **b**, Optical configuration for Scanning Angle Interference Microscopy (SAIM); the boundary of the glycocalyx is marked by fluorescent labeling of the plasma membrane, whose position is localized using axially varying patterns of structured illumination generated through interference of direct and reflected laser light. Silicon (Si) chips with a layer of oxide (SiO) serve as both the optical mirror and cell substrate. **c**, Proposed membrane labelling strategy in this work using leucine zipper pairs (Azip and Bzip). Azip is conjugated with fluorescent protein or dye. Bzip is genetically encoded and expressed as a fusion protein with the PDGFRβ transmembrane (TM) domain.
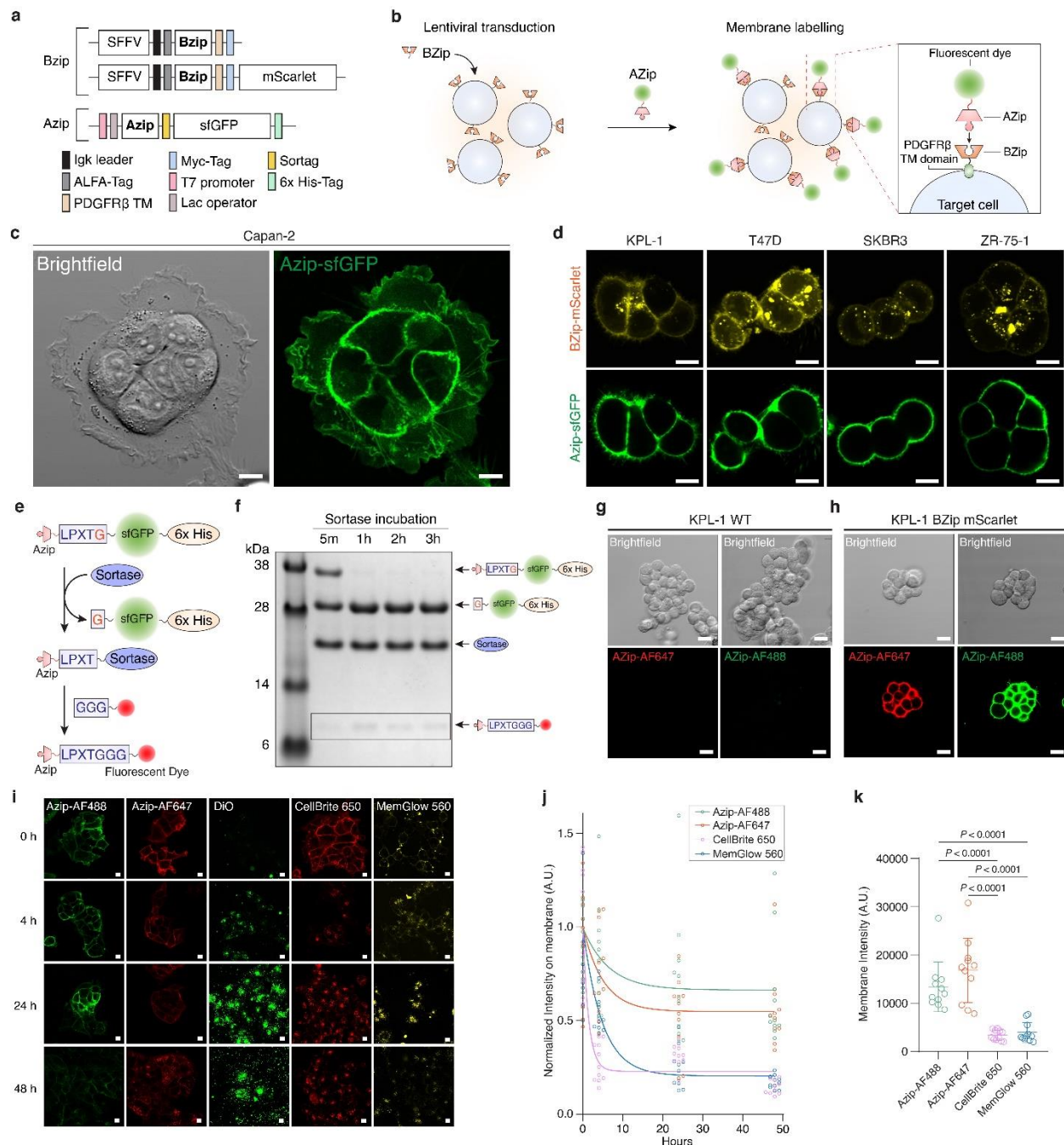
Figure 2: Validation of the leucine zipper-based membrane labelling strategy. a, Schematic representation of constructs used to make Bzip-PDGFRβ TM constructs and Azip-Sortag-sfGFP construct. **b**, Schematic representation of cell membrane labelling using Azip-Bzip interaction. **c**, Fluorescence and bright-field images of Bzip-overexpressing Capan-2 pancreatic cancer cells with 1 µM Azip-sfGFP for 1 hour at 4°C. Scale bars, 10 µm. **d**, Fluorescence images of Bzip-mScarlet and Azip-sfGFP on indicated cancer cell lines for 1 hour at 4°C. Scale bars, 10 µm. **e**, Schematic of sortase-mediated reaction on Azip-sortag-sfGFP to replace the fluorescent protein with a small organic fluorophore. **f**, Coomassie blue staining analysis of sortase-mediated modification of Azip-

sortag-sfGFP to yield Azip-Alexa Fluor 647 (AF647). **g, h**, Fluorescence and bright-field images of KPL-1 wild-type (**g**) and Bzip-overexpressing KPL-1 breast cancer cells (**h**) double labeled with Azip-AF488 and Azip-AF647 (1:100 dilution) for 1 hour at 4°C. Scale bars, 10 µm. **i,** Representative fluorescence microscopy of Bzip-expressing KPL-1 cells labeled with various membrane stains: Azip-AF488, Azip-AF647, DiO, CellBrite 650, or MemGlow 560 according to manufacturers' recommended buffer compositions and concentrations. Cells were stained for 10 minutes at 37°C followed by two washes with culture medium. **j**, Quantification of normalized membrane fluorescence intensity over time (20×20 pixel regions, 2.98×2.98 µm) averaged from minimum 11 cells per condition. **k**, Membrane fluorescence intensity of each dye immediately after labelling (time 0). In **k**, statistical analysis was performed by one-way ANOVA with Tukey's post hoc tests.
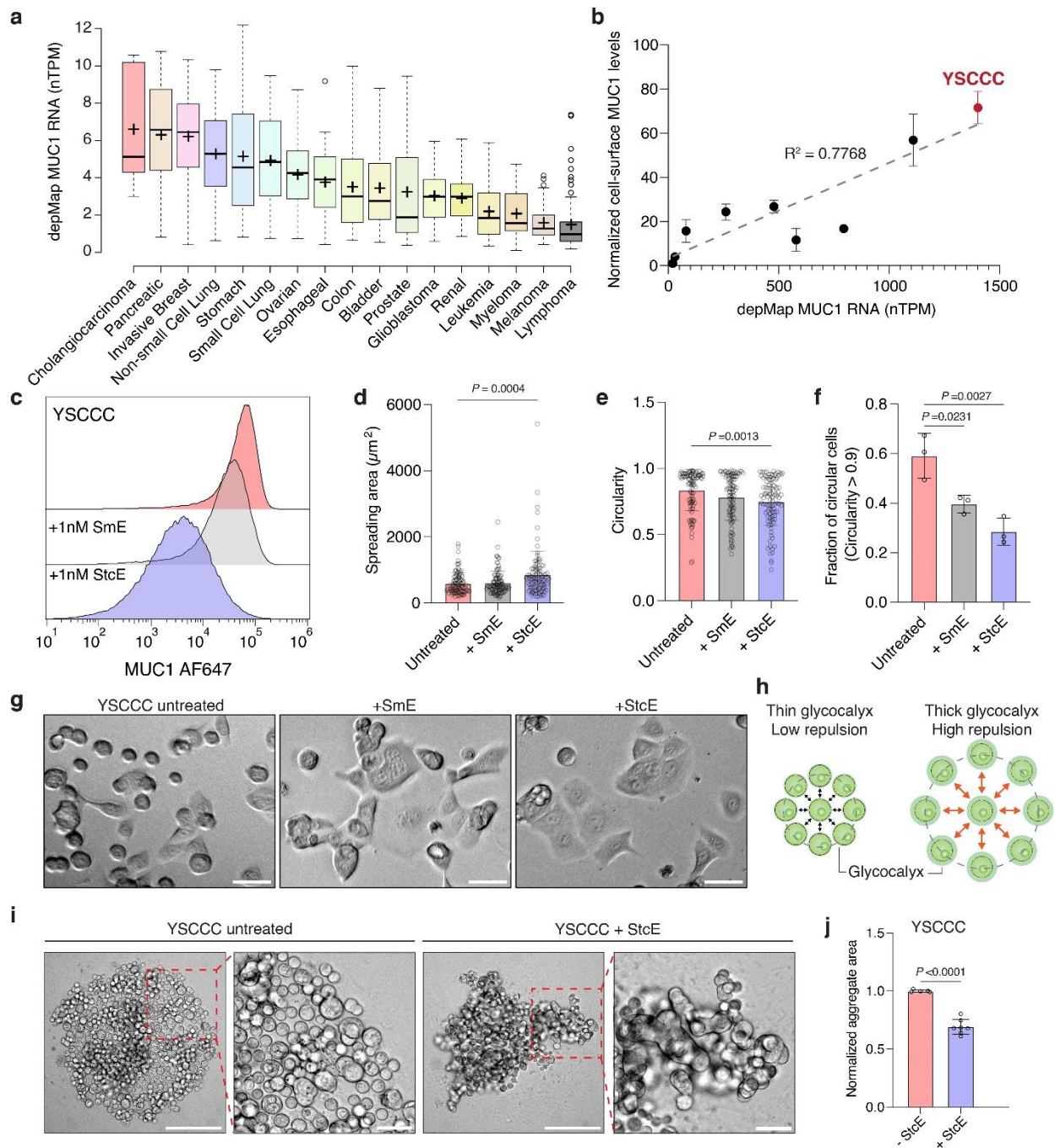
Figure 3: Cholangiocarcinoma cell line YSCCC exhibits high MUC1 surface expression. a, MUC1 transcript levels as measured by the depMap project for the indicated cancer categories; center lines show the medians; means are indicated by '+'; box limits indicate the 25th and 75th percentiles; whiskers extend 1.5 times the interquartile range from the 25th and 75th percentiles, outliers are represented by dots. n = 8, 50, 49, 85, 35, 47, 58, 25, 44, 27, 8, 42, 30, 79, 29, 47, 74 sample points. **b**, Linear correlation between MUC1 transcript levels as measured by the depMap project and MUC1 surface levels as measured by flow cytometry. Points plotted as mean ± s.d.

measured from at least 2 independent experiments. Data for the cholangiocarcinoma cell line, YSCCC, is shown in red. **c**, Representative flow cytometry histograms showing MUC1 levels in YSCCC cells following overnight treatment with 1 nM SmE and 1 nM StcE. **d,e**, Quantification of spreading area (**d**) and circularity (**e**) of YSCCC cells following adhesion overnight to tissue culture flasks. Results are the mean ± s.d. of n = 100 cells per condition. **f**, Quantification of the fraction of highly circular cells across n = 3 fields of view from phase contrast images from **e**. Highly circular cells were determined as those with a circularity value > 0.9. **g**, Representative phase-contrast images of overnight attachment of YSCCC cells in either the presence or absence of 1 nM SmE or 1 nM StcE (scale bar, 50 μm). **h**, Schematic of predicted behavior of cell-cell repulsion in multicellular aggregate formation assays. **i**, Representative brightfield images of multicellular aggregates formed by seeding 1,000 cells of YSCCC per well in round bottom, ultra-low adhesion wells in either the presence or absence of 10 nM stcE for 24 hours. Scale bar = 200 μm, inset scale bar = 50 μm. **j**, Quantification of overall aggregate area, normalized to untreated YSCCC. Results are the mean ± s.d. of n = 5 aggregates for untreated, n = 7 aggregates for StcE treated. Statistics were determined using a two-tailed Student's t-test. In **d,e,f**, statistics were determined using a one-way ANOVA with Tukey's multiple comparisons test.
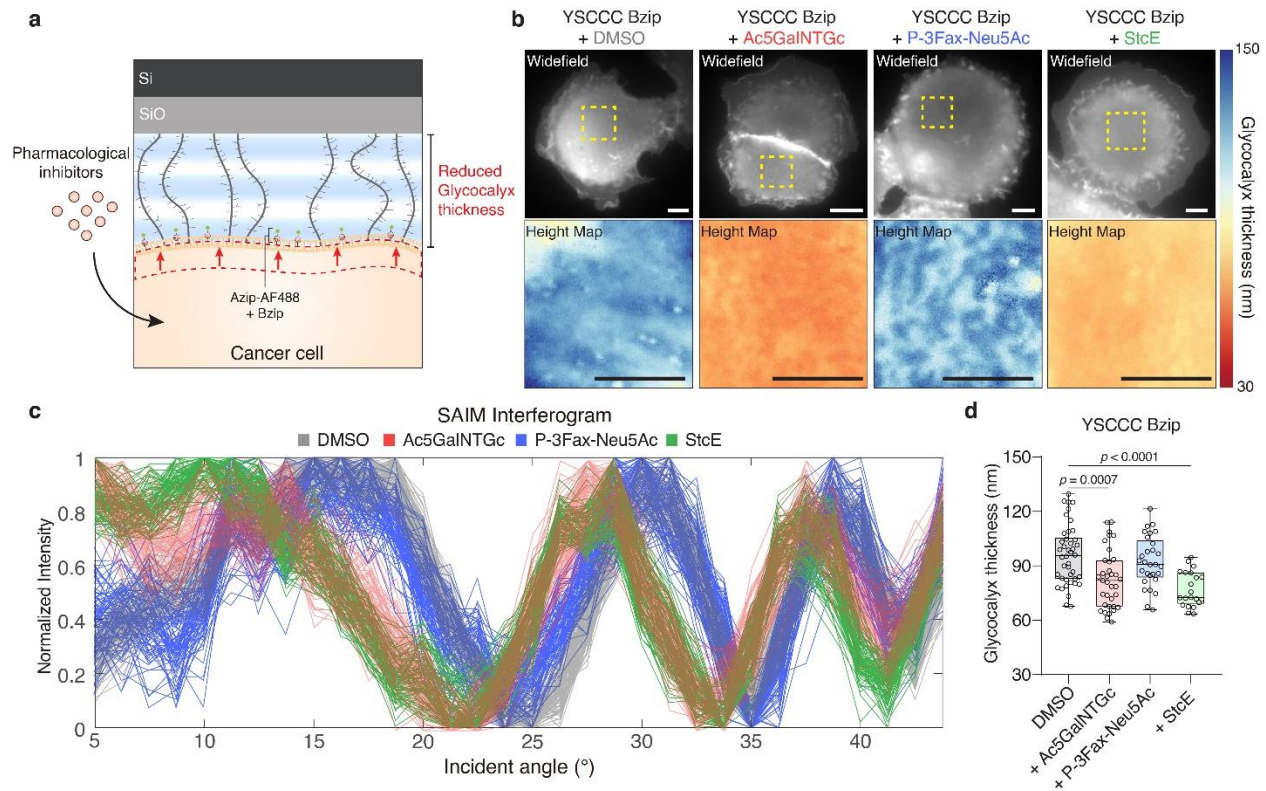
Figure 4: Pharmacological inhibitor screening using leucine zipper-based SAIM. a, Schematic representation of glycocalyx thickness reduction by pharmacological inhibitors as detected by leucine zipper-based SAIM. **b**, Representative wide-field image and glycocalyx thickness map of live YSCCC expressing Bzip construct labeled with Azip-AF488 (1:100 dilution) following treatment with the indicated inhibitors;100 μM Ac$_5$GalNTGc, 100 μM P-3Fax-Neu5Ac for 48 hours or 100 nM StcE mucinase for 1 hour at 37°C. Scale bars, 10 μm. **c**, Representative pixelwise SAIM interferograms for each condition in **b. d**, Quantification of glycocalyx thickness in YSCCC cells expressing Bzip treated with the indicated inhibitors. Boxes and whiskers show the first and third quartiles (boxes), median, and range of the data. Each condition includes a minimum of n = 21 cells from a representative experiment. In **d**, statistical analysis was performed by one-way ANOVA with Tukey's post hoc tests.
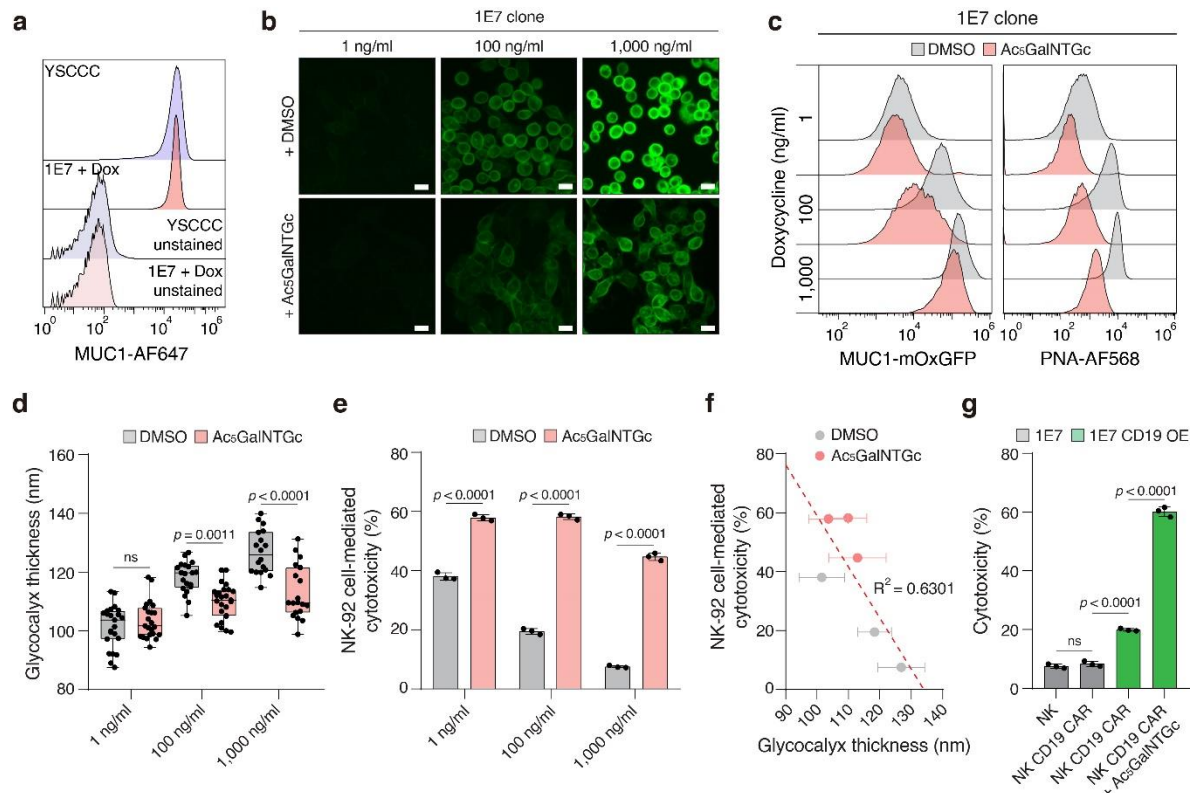
Figure 5: Inhibition of O-glycan biosynthesis enhances NK and CAR-NK cell-based cytotoxicity *in vitro*. a, Representative flow cytometry analysis comparing MUC1 surface levels between YSCCC cells and stable cell clone with titratable expression of MUC1 ectodomain (1E7 clone) induced with 1 µg/mL doxycycline for 24 hours. **b**, Fluorescence images of 1E7 cells induced at the indicated concentration of doxycycline with DMSO or 100 µM Ac$_5$GalNTGc inhibitors for 48 hours. Scale bar, 200 µm. **c**, Flow cytometric analysis of MUC1 mOxGFP expression and PNA binding in 1E7 cells treated with DMSO or 100 µM Ac$_5$GalNTGc for 48 hours at indicated doxycycline concentrations. **d**, Quantification of glycocalyx thickness in 1E7 cells treated with DMSO or 100 µM Ac$_5$GalNTGc for 48 hours at indicated doxycycline concentrations. The boxes and whiskers show the first and third quartiles (boxes), median and range of data. Each condition includes a minimum of 18 cells from a representative experiment ($n = 3$ independent experiments). **e**, NK-92-cell-mediated cytotoxicity against the wild-type and engineered 1E7 cells at the indicated doxycycline induction level. NK-cell-to-target-cell ratio is 5:1. Results are mean ± s.d. of n = 3 technical replicates for one representative of three independent experiments. **f**, Correlation between NK-92 cell cytotoxicity and glycocalyx thickness (R^2 = 0.6301); data from panels **d** and **e**; dashed line indicates linear regression; the dashed line indicates a linear fit to the data. **g**, NK-92 and CD19 CAR NK-92-cell-mediated cytotoxicity against 1E7, CD19 OE 1E7, or 100 µM Ac$_5$GalNTGc treated 1E7 cells at 1,000 ng/ml of doxycycline concentrations. Results are mean ± s.d. of n = 3 technical replicates. In **d**, **e**, and **g**, statistical analysis was performed by one-way ANOVA with Tukey's post hoc tests.
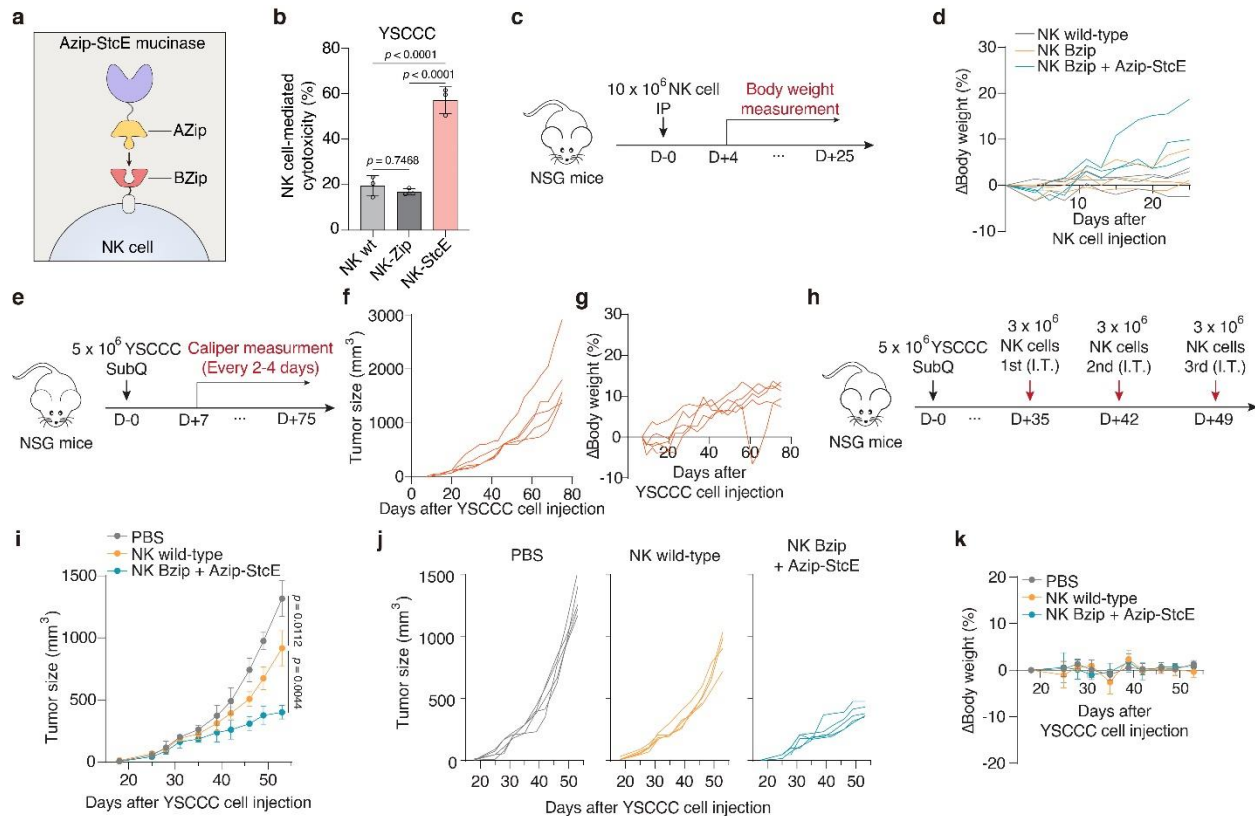
Figure 6: Safety evaluation and anti-tumor activity of StcE-NK cells in YSCCC xenograft model. a, Cartoon showing the design of NK cells tethering with StcE cells (StcE-NK) using leucine zippers. **b**, Killing of YSCCC cells by NK-92, NK-92 expressing Bzip construct (NK-Zip), and NK-Zip tethered with StcE. NK-cell-to-target-cell ratio is 10:1. Results are mean ± s.d. of n = 3 technical replicates. **c**, Schematic of experimental setup in which 10×10^6 cells of NK cell, Bzip overexpressing NK cell, or StcE-NK were treated intraperitoneally in the flank of NSG mice. **d**, Change in body weight over as measured (n = 3 mice per condition). **e**, Schematic of experimental setup in which 5×10^6 YSCCC cells were subcutaneously implanted in the flank of NSG mice. **f,g**, Tumor volume (**f**) and change of body weight (**g**) over time as measured by caliper (n = 5 mice). **h**, Schematic of experimental setup in which 5×10^6 YSCCC cells were subcutaneously implanted in the flank of NSG mice. Mice were treated intratumorally with PBS, 3×10^6 wild-type NK-92 cells, or 3×10^6 StcE-NK cells three times. **i-k**, Tumor volume (**i,j**) and change of body weight (**k**) over time as measured by caliper (n = 5 mice per treatment group). In **b and i**, statistical analysis was performed by one-way ANOVA with Tukey's post hoc tests (**b**) and two-way ANOVA with correction for multiple comparisons (**i**).